ACS Catalysis

Research Article

pubs.acs.org/acscatalysis

Formation of Cu Nanoparticles in SBA-15 Functionalized with Carboxylic Acid Groups and Their Application in the Water−Gas Shift Reaction

Ching S. Chen,*[,†] Yuan T. Lai,[†] Tzu W. Lai,[†] Jia H. Wu,[†] Ching H. Chen,[†] Jyh F. Lee,[‡] and Hsien M. Kao*[,§]

[†]Center for General Education, Chang Gung University, 259 Wen-Hwa first Road, Kwei-Shan, Taiwan, 33302, Republic of China

[‡]National Synchrotron Radiation Research Center, Hsinchu 300, Taiwan, Republic of China

[§]Department of Chemistry, National Central University, Chung-Li, Taiwan 320, Republic of China

Supporting Information

ABSTRACT: SBA-15 functionalized with carboxylic acid groups has been used to synthesize Cu nanoparticles 2−6 nm in average size with 7.6−25.2 wt % Cu. In this study, the formation mechanism and characterization of Cu nanoparticles at various Cu concentrations are described. For samples with 7.6 and 11.9 wt % Cu, linear $[Cu^{\delta+}\cdots O^{\delta-}\cdots Cu^{\delta+}]_n$ chains generated through calcination are possibly located inside the SBA-15 channels. When the concentration of Cu is increased to 18.3 wt %, the $Cu_2(OH)_3NO_3$ species becomes the dominant intermediate before bulky CuO is formed. It is found that the average 2-nm Cu particles provided a significantly higher turnover rate for water−gas shift (WGS) reaction than did higher Cu contents on SBA-15. We propose that the highly dispersed Cu particles or isolated Cu atoms on Cu/SBA-15 catalysts can serve as major active sites for the WGS reaction. The 7.6 and 11.9 wt % Cu/SBA-15 catalysts provide abundant sites on highly dispersed Cu particles or isolated Cu atoms, which lead to a highly efficient WGS reaction.

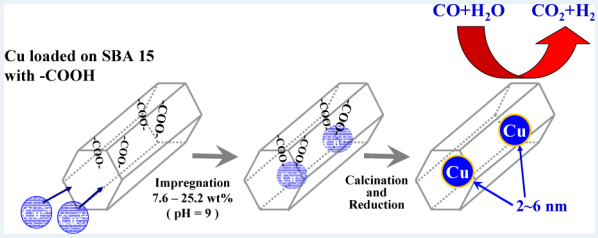

KEYWORDS: *water-gas shift reaction, carboxylic acid, Cu nanoparticles*

1. INTRODUCTION

Copper-based catalysts are frequently used in industrial-scale petrochemical catalytic processes, including methanol synthesis, steam reforming of methanol to produce H_2 for fuel cells, CO oxidation and low-temperature water−gas shift (WGS) reactions. The particle size, the surface structure, the number of active sites, and the location of metal centers can determine the selectivity and activity of catalytic reactions. To date, preparations of small metallic particles have been extensively investigated and are viewed as an active area of research in solid-state physics and chemistry. Nanoparticles usually offer a larger surface-to-volume ratio and a higher concentration of partially coordinated surface sites than bulk materials and consequently appear to possess different physical and chemical properties.[1,2] Several groups have reported that a reduction in the particle size of metals changes the electronic structure and the distribution of surface sites, which leads to enhanced catalytic activity.[3−5] Recently, Qiao et al. have stated that isolated single Pt atoms can lead to extremely high efficiency for CO oxidation.[6]

In reality, conventionally supported catalysts are prepared by wet chemical methods that generate small and dispersed active catalytic sites; however, such synthetic methods do not always allow control of the size distribution. Extensive efforts have been made to control dispersions on supported catalysts, but the development of a simple methodology for the preparation of highly dispersed metal particles still remains a challenge. The discovery of mesoporous materials, such as MCM-41, MCM-48, and SBA-15, has opened new opportunities for applications of these materials as catalyst supports.[7−10] Recently, mesoporous SBA-15 silica has become a promising support for metal particles because of its high surface area (600−1000 m^2/g). SBA-15 possesses a hexagonal structure of uniform channels with pore diameters in the range of 5−30 nm, which are much larger than those of MCM-41 and MCM-48 and therefore exhibits a significantly lower diffusion resistance.[9] Reports on the synthesis of copper-containing mesoporous materials have been published in the literature.[11−13] Several mesoporous materials have become widely available as catalytic supports to produce Cu nanoparticles directly from the synthesis of mesoporous materials.[14−19] However, the synthesis of Cu particles with diameters less than 4 nm on porous supports with high Cu loadings (>10 wt %) can be difficult because Cu particles easily undergo sintering upon thermal treatments, such as calcination and reduction.

Received: January 17, 2013
Revised: February 20, 2013
Published: February 27, 2013

The functionalization of mesoporous silica materials with organic functional groups has enabled new applications for these materials. Here, we report a simple wet impregnation method to obtain Cu nanoparticles in carboxylic-acid-(−COOH) functionalized SBA-15 under a high Cu loading. A pure SBA-15 material without −COOH groups cannot effectively bind Cu^{2+} ions in the pore structure; however, the synthesized −COOH-functionalized SBA-15 materials can capably remove Cu^{2+} ions from water.[20] The actual amount of Cu^{2+} adsorption may be limited by the number of surface carboxylic groups present. The Cu^{2+} ions trapped in the structure of SBA-15 can be further transformed to nanosized Cu particles through calcination and reduction pretreatments.

The WGS reaction is used extensively in the conversion of fossil fuels to hydrogen. It converts CO to CO_2, which is an important process if hydrogen is to be used as a clean fuel for proton-exchange membrane fuel cells (PEMFC) because CO has a strong poisoning effect on Pt-based anodes. Nanoscale copper particles are expected to exhibit catalytic behavior that differs from that of traditional Cu-based catalysts for CO removal in the WGS reaction.[21−26] The aim of this research is to chemically characterize the Cu nanoparticles in each pretreatment step, including impregnation, calcination, and reduction. Attention is focused on the identification, chemical state, and structure of Cu species in SBA-15. Nanoscale Cu particles in SBA-15 have been reported to exhibit high efficiency when used as a catalyst for the WGS reaction. The active sites for CO adsorption are discussed in relation to the reaction rate of the Cu/SBA-15 catalysts.

2. EXPERIMENTAL SECTION

2.1. Catalyst Preparation. The synthesis of −COOH-functionalized mesoporous silica with SBA-15 motifs was performed according to the method reported in our previous study.[20] One gram of the triblock copolymer Pluronic P123 was dissolved in 31.25 g of 1.9 M HCl and was stirred for 4 h at 313 K. Premixed tetraethoxysilane (TEOS) from Aldrich and 25 wt % carboxyethylsilanetriol (CES) in water from Gelest were added dropwise to the solution with vigorous stirring for 20 h at 313 K. The milky reaction mixture was subsequently hydrothermally treated at 373 K for 24 h. The composition of the reaction mixture was 0.1 CES: 0.9 TEOS: 0.0168 P123: 5.85 HCl: 162.68 H_2O. The resultant precipitate was collected by filtration, washed with water, and air-dried at room temperature. Template removal was accomplished by suspending 1.5 g of the synthesized material in 400 mL of an HCl−ethanol mixture at 351 K for 24 h, and the procedure was repeated once. The product was washed with water and dried at 363 K. The Cu/SBA-15 catalysts were prepared by impregnating SBA-15 that contained carboxylic acid groups with 20 mL of an aqueous solution of $Cu(NO_3)_2{\cdot}2.5H_2O$ at pH = 9. The solid was collected by filtration and was subsequently air-dried at 353 K for 10 h. Copper nanoparticles were obtained after calcination of the samples in air and reduction in H_2 at 573 K for 5 h. The commercial $Cu/ZnO/Al_2O_3$ catalyst was manufactured by Süd-Chemie Catalysts (catalyst #G66B) and had a molar Cu/Zn/Al ratio of 30:60:10.

2.2. H_2 Temperature-Programmed Reduction (H_2-TPR). H_2-TPR of the catalysts was performed at atmospheric pressure in a conventional flow system. The Cu/SBA-15 catalyst was placed in a tube reactor and heated at a rate of 10 K/min in a 10% H_2/N_2 mixed gas stream flowing at 30 mL/min. The TCD current was 80 mA, and the detector temperature was 373 K. A cold trap that contained a gel formed by the addition of liquid nitrogen to isopropanol in a Thermos flask was used to prevent water from entering the TCD.

2.3. Measurement of FT-IR spectra. In situ DRIFT analysis of CO adsorption and the temperature-dependent analysis of Cu/SBA-15 in air were performed with a Nicolet 5700 FTIR spectrometer fitted with a mercury−cadmium−telluride (MCT) detector; the instrument was operated at 1 cm^{-1} resolution with 256 scans. The DRIFT cell (Harrick) was equipped with ZnSe windows and a heating cartridge that allowed samples to be heated to 773 K. The IR spectra of CO adsorption on Cu/SBA-15 was obtained using pure CO that was passed through Cu/SBA-15 for 30 min at room temperature, and residual gaseous CO was purged for 60 min. All Cu/SBA-15 samples were pretreated by calcination in air and reduction in H_2 gas at 573 K for 5 h.

2.4. In Situ X-ray Absorption Spectra (XAS) Measurements. XAS spectra were recorded at the BL17C1 beamline at the National Synchrotron Radiation Research Center (NSRRC), Taiwan, where the electron storage ring is operated at 1.5 GeV. A double Si(111) crystal monochromator was employed for energy selection with a resolution ($\Delta E/E$) greater than 1×10^{-4} at the Cu K-edge (8979 eV). All XAS powder studies for the nanoparticles were conducted in a homemade cell built from stainless steel. Two holes were made in the cell, one on the top of the cell and the other on one side. After the solid samples were placed inside the cell, the holes were closed with Kapton film to avoid exposure of the sample to the atmosphere. All spectra were recorded at room temperature in transmission mode. Higher harmonics were eliminated through detuning of the double Si (111) crystal monochromator. Three gas-filled ionization chambers were used in series to measure the intensities of the incident beam (I_0), the beam transmitted by the sample (I_t), and the beam subsequently transmitted by the reference foil (I_r). The third ion chamber was used in conjunction with the reference sample, which was a Cu foil, for Cu K-edge measurements. The parameters for extended X-ray absorption fine structure (EXAFS) measurements, data collection modes, and error calculations were all controlled according to guidelines set by the International XAFS Society Standards and Criteria Committee.

EXAFS data reduction was conducted using standard procedures. The EXAFS function χ was obtained by subtracting the post-edge background from the overall absorption and normalizing with respect to the edge jump step. The normalized $\chi(E)$ was transformed from energy space to k-space, where k is the photoelectron wave vector. The $\chi(k)$ data were multiplied by k^3 for the Cu K-edge to compensate for the damping of EXAFS oscillations in the high k-region. Subsequently, the $\chi(k)$ data in the k-space that ranged from 3.84 to 11.5 $Å^{-1}$ for the Cu K-edge were Fourier transformed (FT) to r-space to separate the EXAFS contributions from different coordination shells. A nonlinear least-squares algorithm was applied to the curve fitting of the EXAFS with phase correlation in the r-space between 1.5 and 3.5 Å for the Cu K-edge, depending on the bond to be fitted. The effective scattering amplitude [$f(k)$] and phase shift [$\delta(k)$] for the Cu−O and Cu−Cu bonds were generated using the FEFF7 code.

The Cu−O shell was based on the Cu_2O cubic structure with $Pn\bar{3}m(O_h^4)$ space symmetry by fixing the Cu atoms at (0, 0, 0), (1/2, 1/2, 0), (1/2, 0, 1/2), and (0, 1/2, 1/2), such that the Cu atoms formed an fcc lattice. The oxygen atoms formed a bcc

dx.doi.org/10.1021/cs400032e | ACS Catal. 2013, 3, 667−677

lattice and occupied positions (1/4, 1/4, 1/4) and (3/4, 3/4, 3/4). The Cu−Cu shell was based on the Cu foil structure with $Fm\bar{3}m$ space symmetry group by fixing the Cu atom at the (0, 0, 0) position in the cubic unit-cell model. The lattice parameter a for the FEFF7 calculation was set to 4.258 Å and 3.615 Å for Cu_2O and Cu foil, respectively. All computer programs were implemented using the UWXAFS 3.0 software package, and the backscattering amplitude and the phase shift for the specific atom pairs were theoretically calculated using the FEFF7 code. From these analyses, structural parameters such as the coordination number (N) and the bond distance (R) were successfully calculated. The amplitude reduction factor (S_0^2) value, which accounts for the energy loss due to multiple excitations, was found by analyzing the Cu foil reference sample and fixing the coordination number in the FEFFIT input file; the value was 0.88 for the Cu K-edge.

2.5. In Situ X-ray Diffraction (XRD) Measurements. In situ XRD measurements for all Cu/SBA-15 samples were performed at the high-energy beamline 01C2 at the National Synchrotron Radiation Research Center (NSRRC), Hsinchu. The beamline was operated at 25 keV, and XRD spectra were recorded at a wavelength of λ = 0.5166 Å. The samples were loaded into a capillary cell that could be heated to 773 K under a flow of air and H_2 gas while the XRD patterns were recorded.

2.6. Measurement of Copper Surface Area. The specific Cu^0 surface area and the dispersion of Cu/SBA-15 and Cu/ZnO/Al_2O_3 catalysts were determined by N_2O oxidation and H_2-TPR. All of the Cu^0 on the Cu/SBA-15 catalysts was carefully oxidized in a 10% N_2O/N_2 stream according to the reaction: $2Cu(s) + N_2O \rightarrow Cu_2O(s) + N_2$. The monolayer of Cu_2O left on the catalyst surface after N_2O oxidation was reduced using a TPR process. The N_2O oxidation was performed with a 10% N_2O/N_2 mixture flowing at 30 mL/min at 353 K. The TPR area of Cu_2O was quantified by sampling 1 mL of 10% H_2/N_2 to calculate the amount of N_2O consumed. The Cu^0 surface area could thus be calculated by assuming a N_2O/Cu molar stoichiometry of 0.5:1. The average surface density for Cu metal is 1.46×10^{19} copper atoms/m^2. The copper content of all catalysts was measured by inductively coupled plasma mass spectrometry (ICP/MS). The dispersion of Cu/SBA-15 and Cu/ZnO/Al_2O_3 catalysts could thus be calculated from the Cu atoms on the surface and the total Cu content of the catalyst.

2.7. Measurements of Turnover Rate. All WGS reactions were performed in a fixed-bed reactor (0.95 cm outer diameter) at atmospheric pressure. A thermocouple connected to a PID temperature controller was placed on top of the catalyst bed. The WGS reactions were performed using a 5% CO stream with a total flow rate of 30 mL/min passed through liquid water at room temperature, and the resulting mixture of CO/H_2O in a 1.1:1 molar ratio was passed over 50 mg of catalyst. The flow system of the reactor was heated with heating belts to avoid the condensation of water. The conversion of WGS reaction was kept below 10% to be close to differential conditions. All products were analyzed by gas chromatography (GC) on a 12-ft Porapak-Q column using a thermal conductivity detector (TCD). The turnover frequency (TOF) was calculated using the formula[27] TOF = [conversion ×0.025 (mL/s for CO) × 6.02 × 10^{23} (molecules/mol)]/[24400 (mL/mol) × 1.46 × 10^{19} Cu sites/m^2)].

2.8. Transmission Electron Microscopy (TEM). High-resolution TEM analysis was carried out on an JEM2000FX II operating at 300 KeV located at the High Valued Instrument Center in the National Central University, Taiwan. The catalyst samples after pretreatment were dispersed in methanol, and the solution was mixed ultrasonically at room temperature. A part of this solution was dropped on the Ni grid for TEM imaging.

3. RESULTS

3.1. H_2 Temperature-Programmed Reduction (H_2-TPR). Figure 1 depicts the H_2-TPR profiles of the CuO/SBA-15 catalysts during the calcination treatment at 573 K for 5 h. Reduction of the samples with 7.6 and 11.9 wt % CuO/SBA-15 occurred at 498 K. Two major peaks with maxima at 523 and 703 K could be observed when the Cu content was increased to 25.2 wt %. The TPR profile of the sample with 25.2 wt % Cu^{2+}/SBA-15 that was not calcined was compared to that of the CuO/SBA-15 samples, which revealed a major reduction peak at 533 K and a shoulder peak at 565 K. In general, a reduction temperature between 473 and 573 K for Cu oxides is attributed to the reduction of Cu^{2+} to Cu^0. The high-temperature reduction peak at 703 K may depend closely on the interaction between Cu^{2+} ions and the support.[28] In our previous study, we showed that pretreatments of calcination in air and reduction in H_2 at 573 K did not deconstruct the SBA-15 template in Cu/SBA-15 samples.[20]

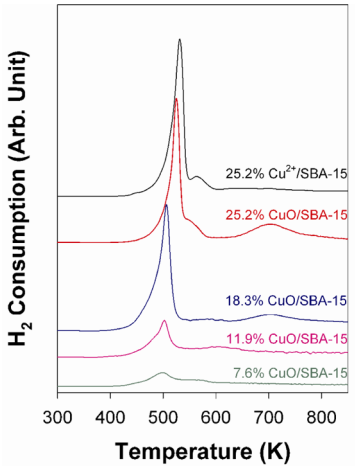

Figure 1. TPR profiles of CuO/SBA-15 samples after calcination in air at 573 K for 5 h.

3.2. UV−vis Diffuse Reflectance Spectroscopy. Figure 2 shows the DR−UV−vis spectra of Cu^{2+}/SBA-15 impregnated with varying Cu contents undergoing calcination at 573 K for 5 h and a standard sample of CuO. The 7.6 wt % Cu/SBA-15 had a broad absorption band at 350−650 nm with absorption maxima at 410 and 500 nm. The broad band at 350−650 nm gradually disappeared as another absorption band formed at 290 nm with increasing Cu content. The UV−vis absorption maxima for Cu oxides in mesoporous materials have already been assigned in the literature; the absorption at 350−650 nm might be related to the presence of linear oligonuclear $[Cu^{\delta+}\cdots O^{\delta-}\cdots Cu^{\delta+}]_n$ clusters.[9,29,30] In addition, CuO powder shows absorption bands at 290, 330, and 895 nm. The strong bands at approximately 895 nm for all samples are due to the $^2E_g \rightarrow {}^2T_{2g}$ transition of Cu^{2+} in an octahedral geometry. The peaks positioned at 290 and 330 nm can be attributed to $Cu^{2+} \leftarrow O^{2-}$ ligand-to-metal charge transfer (LMCT) between oxygen and isolated Cu^{2+} ions in the CuO structure.

dx.doi.org/10.1021/cs400032e | ACS Catal. 2013, 3, 667−677

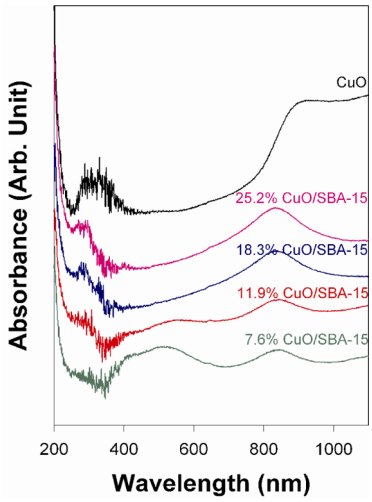

Figure 2. UV−vis diffuse reflectance spectra of CuO/SBA-15 samples and CuO powder.

3.3. In Situ XRD Spectroscopy. The XRD spectra of the impregnated Cu^{2+}/SBA-15 samples during calcination are shown in Figure 3. All spectra were recorded in situ under an

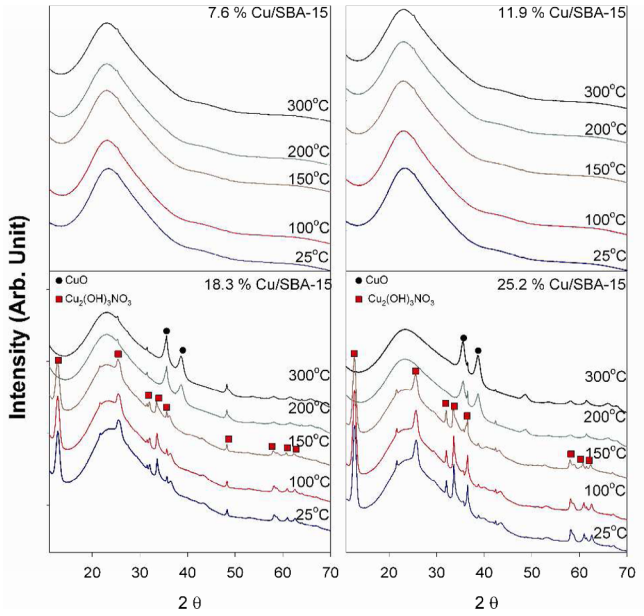

Figure 3. In situ XRD spectra of impregnated Cu^{2+}/SBA-15 in air at various calcination temperatures.

air stream. The XRD spectra for the samples impregnated with 7.6 and 11.9 wt % Cu had no obvious diffraction peaks before or after calcination. However, several diffraction patterns could be observed in Cu^{2+}/SBA-15 samples with higher Cu^{2+} contents (18.3 and 25.2 wt %). These diffraction peaks indicated the formation of monoclinic $Cu_2(OH)_3NO_3$ crystals during Cu^{2+} ion impregnation.[31] The characteristic peaks for the $Cu_2(OH)_3NO_3$ species gradually vanished with increasing temperature and transformed into monoclinic CuO peaks (35.6° and 38.7°) at temperatures greater than 523 K. Nevertheless, the characteristic peaks for the $Cu_2(OH)_3NO_3$ species did not fully disappear upon formation of CuO, even when the calcination temperature was maintained at 573 K for 1 h.

Figure 4 shows the XRD spectra of the 5−15 wt % Cu^{2+} SBA-15 sample without −COOH groups on SiO_2 at a pH of 9; the spectra reveal that the apparent crystal structure of $Cu_2(OH)_3NO_3$ could be observed in the XRD patterns.

Figure 5 shows the in situ XRD spectra of the calcined CuO/SBA-15 samples undergoing a TPR. For the samples with 7.6 and 11.9 wt % CuO on SBA-15, the broad peak at 43.4° for the (111) plane of metallic Cu was formed at 463 K; the intensity of this peak gradually increased with increasing reduction temperature. The XRD spectra for the reduced samples with 18.3 and 25.2 wt % CuO shown in Figure 5 revealed several diffraction peaks for the reduced metallic Cu crystals at temperatures greater than 463 K: 43.3° for (111), 50.2° for (200), 73.8° for (220), and 89.4° for (311) planes. The emergence of these diffraction peaks was accompanied by the disappearance of peaks attributed to monoclinic CuO particles on SBA-15. However, the residual diffraction peaks belonging to $Cu_2(OH)_3NO_3$ still could be observed on the 18.3 and 25.2 wt % Cu/SBA-15. The average particle size of all the reduced Cu/SBA-15 samples was calculated from the Cu(111) peak according to the Scherrer equation using the full-width at half-maximum (fwhm) values. Samples with less than 11.9 wt % Cu exhibited small particle sizes (approximately 2 nm); however, samples with 18.3 and 25.2 wt % Cu exhibited average particle sizes of 4 and 6 nm, respectively.

3.4. TEM Images. In the TEM images of the catalyst with 25.2 wt % Cu (shown in Figure 6), the Cu particles were clearly located inside the pores of the SBA-15 support (Figure 6A). On the other hand, the EDX spectrum of the channel walls also could find significant Cu signals (Figure 6B), implying that a highly dispersed Cu phase might have high possibility to form inside the pores. In reality, it was difficult to find Cu particles agglomerated on the SBA-15 samples with low Cu content using TEM, but the Cu signal was still present on the channel walls in the EDX spectra.

3.5. X-ray Absorption Near-Edge Structure (XANES). In XAS, the energy region in the vicinity of the absorption edge (0−50 eV) is referred to as XANES; to a large extent, it is a fingerprint for the oxidation state and site symmetry of the element from which the absorption spectrum is measured. Figure 7 shows the Cu K-edge XANES and the first derivative spectra of the impregnated Cu/SBA-15 samples with varying Cu loading. The same shape was observed for XANES spectra and derivative spectra of all impregnated Cu/SBA-15 samples irrespective of the Cu loading. In the pre-edge region, an extremely weak peak at about 8977.6 eV was observed. This peak was assigned to the formally dipole-forbidden Cu^{2+} 1s→3d electronic transition and could be distinguished from the peaks of Cu^{2+} complexes with tetragonal symmetry (D_{4h}), such as square planar or square bipyramidal coordination.

The XANES spectra of CuO and Cu/SBA-15 samples undergoing calcination at 573 K for 5 h are shown in Figure 8. The XANES spectra of the calcined Cu/SBA-15 samples exhibited features that were distinctly different from the spectra of CuO powder. The maxima of the first derivative function of the rapidly rising edge step of all the calcined Cu/SBA-15 samples were positioned at about 8985.5 eV, which is higher than the maximum of CuO at 8983.8 eV. These results suggest that Cu oxides on SBA-15 did not completely match the CuO structure.

Figure 9 reveals the XANES spectra of reduced Cu/SBA-15 samples with varying Cu contents. The spectra of Cu foil and Cu_2O powder were compared with the oxidation states of these

dx.doi.org/10.1021/cs400032e | ACS Catal. 2013, 3, 667−677

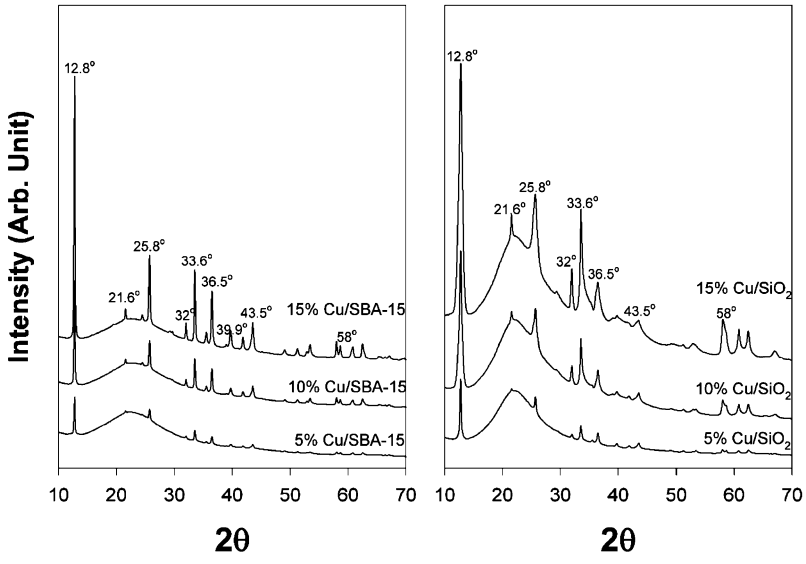

Figure 4. XRD spectra of impregnated Cu^{2+} loaded on pure SBA-15 without −COOH and SiO_2.

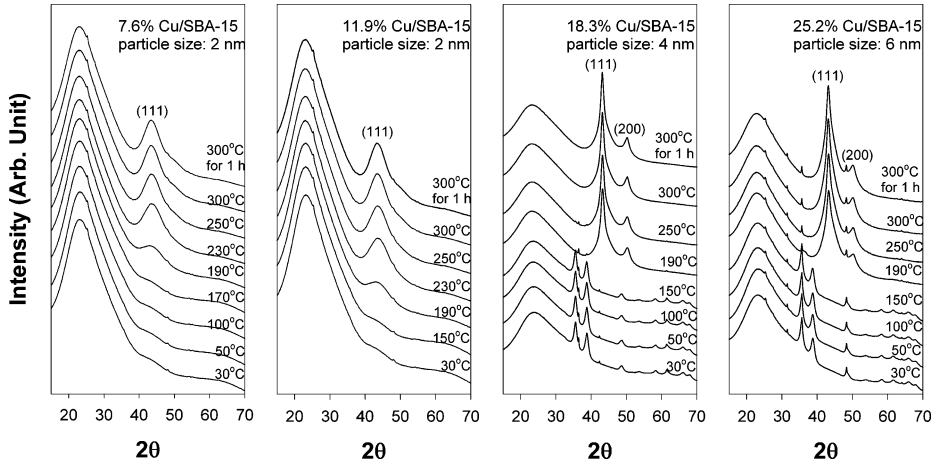

Figure 5. In situ XRD spectra of CuO/SBA-15 in H_2 at various temperatures.

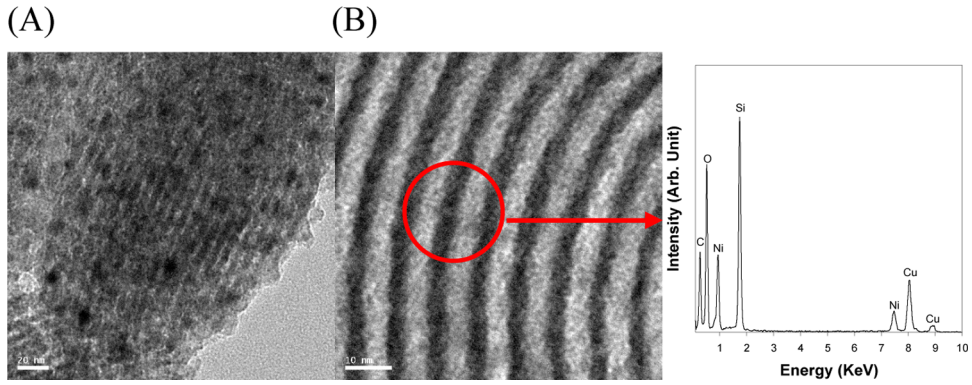

Figure 6. TEM images and EDX spectrum of 25.2 wt % Cu/SBA-15.

reduced Cu/SBA-15 samples. The shape of the spectra changed depending on the Cu loading of the SBA-15 materials. In general, the edge positions were used to determine the oxidation state of the Cu species, which shifted to higher energies as the extent of oxidation increased. Notably, the edge position of the XANES spectrum of the reduced Cu/SBA-15 samples shifted to higher energy when the Cu content was increased to 18.3 wt %. Evidence of these changes was obtained by calculating the first-derivative curves of the XANES spectra. The peaks of the derivative spectra of Cu foil and Cu_2O powder were 8979 and 8981 eV, respectively. On the basis of the derivative spectra, samples with lower Cu loadings (7.6 and 11.9 wt %) appear to contribute to the formation of metallic Cu species. The derivative peaks for samples with a Cu content

dx.doi.org/10.1021/cs400032e | ACS Catal. 2013, 3, 667−677

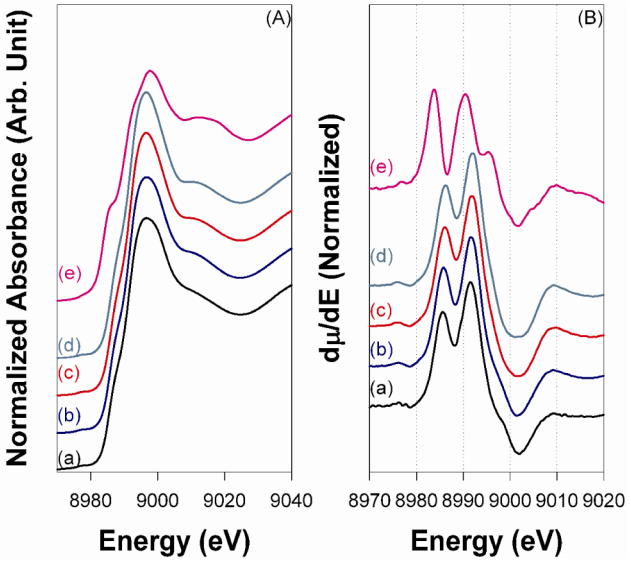

Figure 7. (A) Cu K-edge XANES spectra of Cu^{2+}/SBA-15 (a) 7.6 wt %; (b) 11.9 wt %; (c) 18.3 wt %; (d) 25.2 wt % and (e) CuO powder. (B) First-derivative spectra of (A).

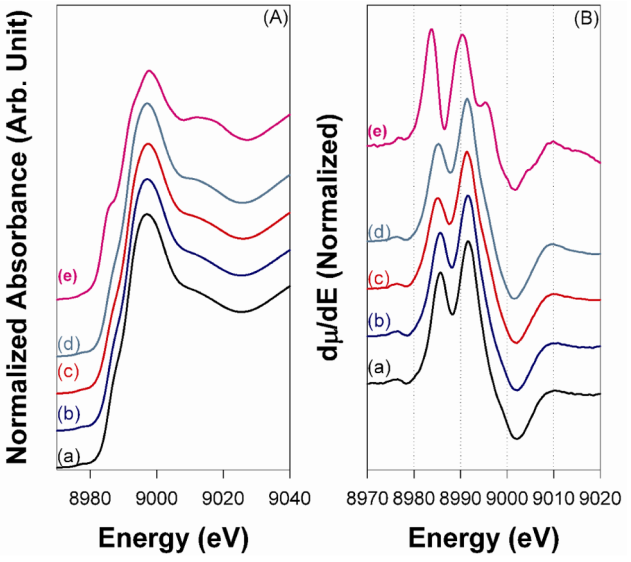

Figure 8. (A) Cu K-edge XANES spectra of CuO/SBA-15 (a) 7.6 wt %; (b) 11.9 wt %; (c) 18.3 wt %; (d) 25.2 wt % and (e) CuO powder. (B) First-derivative spectra of (A).

greater than 18.3 wt % matched those of the Cu_2O powder, which indicated that Cu oxides may form in the reduced Cu structure. The major difference between the Cu_2O and Cu was a prominent feature at approximately 8981−8984 eV seen in the spectrum of Cu_2O; this feature appeared in the absorption region at the higher energy end within the rising edge (denoted as A and B). Peaks A and B were attributed to the $1s\rightarrow 4p_{x,y}$ and $1s\rightarrow 4p_z$ electronic transitions of Cu, respectively.[32,33] In general, the near-edge fine structure of a linear Cu^+ with two coordinated ligands is characterized by a sharp absorption peak between 8980 and 8950 eV (peak A in Figure 9).

3.6. Cu K-edge EXAFS. The FT k^3-weighted EXAFS results at the Cu K-edge, with phase correlation for the impregnated, calcined and reduced Cu/SBA-15 samples with different Cu loadings, are shown in Figure 10. The $k^3x(k)$ spectra were obtained through a comparison of the FEFF theoretical fit with

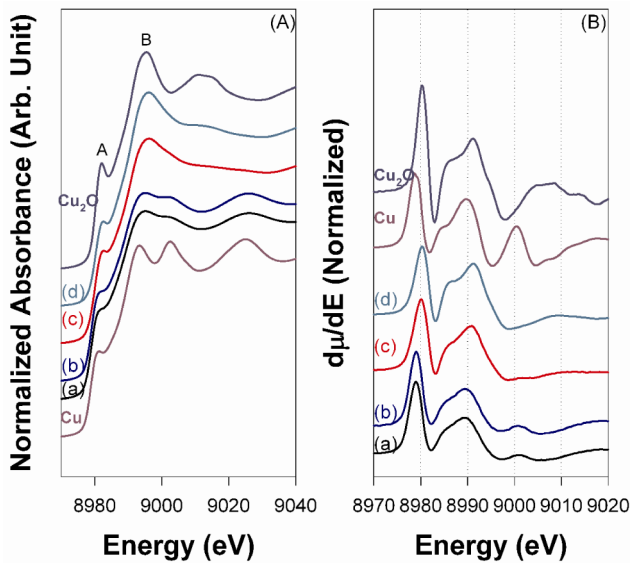

Figure 9. (A) Cu K-edge XANES spectra of Cu/SBA-15 at (a) 7.6 wt %; (b) 11.9 wt %; (c) 18.3 wt %; (d) 25.2 wt %. (B) First-derivative spectra of (A).

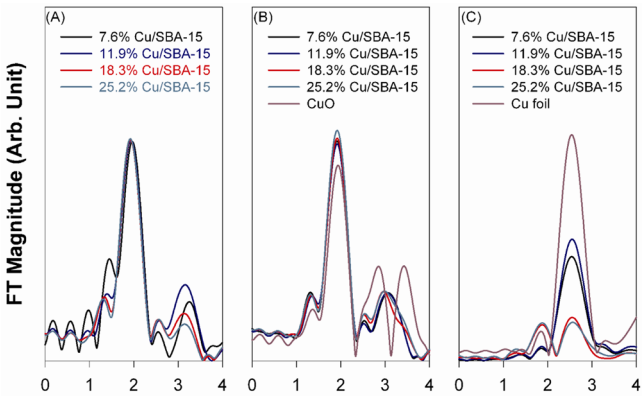

Figure 10. Fourier transforms of EXAFS spectra for (A) as-impregnated Cu^{2+}/SBA-15, (B) calcined CuO/SBA-15, and (C) reduced Cu/SBA-15 samples.

the back-transformed experimental EXAFS data. The two-shell theoretical fit (scatter line) matched closely with the back-transformed experimental data (solid line), as shown in Supporting Information, Figures S1−S3. The structural parameters of the impregnated, calcined and reduced Cu/SBA-15 samples extracted from the best-fit EXAFS data are listed in Tables 1, 2, and 3, respectively.

In Table 1, the coordination number of N_{Cu-O} was found to be about 4.0, and the Cu−O distances were 1.98 Å. However, data on Cu−Cu bonding could not be effectively analyzed from the EXAFS spectra. The effective coordination numbers and interatomic distances of the impregnated Cu/SBA-15 calcined at 573 K for 5 h are listed in Table 2. Compared with the results in Table 1, the coordination number of N_{Cu-O} for all the calcined Cu/SBA-15 samples remained constant at 4.0; however, the Cu−O bond distances were slightly reduced to 1.94 Å. The Cu−Cu bonding information could only be obtained for the samples with 18.3 and 25.2 wt % Cu loadings; both samples exhibited a bond distance of 3.02 Å, and coordination numbers of 1.4 and 1.8 were obtained for the samples with 18.3 wt % and 25.2 wt % Cu, respectively. The

dx.doi.org/10.1021/cs400032e | ACS Catal. 2013, 3, 667−677

Table 1. Structural Parameters of As-Impregnated Cu^{2+}/SBA-15

Cu loading (%)	shell	N	R (Å)	r^a	σ^2 (Å^2)^b	ΔE_0 (eV)^c
7.6	Cu−Cu					
11.9	Cu−Cu					
18.3	Cu−Cu					
25.2	Cu−Cu					
7.6	Cu−O	4.0	1.98	0.020	0.0094	9.2
11.9	Cu−O	4.0	1.98	0.004	0.0049	4.7
18.3	Cu−O	3.9	1.98	0.001	0.0064	2.4
25.2	Cu−O	3.9	1.98	0.001	0.0084	1.1

^{a}Residual factor. ^{b}Debye−Waller factor. ^{c}The inner potential correction.

Table 2. Structural Parameters of Calcined CuO/SBA-15

Cu loading (%)	shell	N	R (Å)	r^a	σ^2 (Å^2)^b	ΔE_0 (eV)^c
7.6	Cu−Cu	7.0	2.51	0.003	0.0016	3.4
11.9	Cu−Cu	7.6	2.52	0.003	0.0026	1.2
18.3	Cu−Cu	2.0	2.55	0.001	0.0101	4.9
25.2	Cu−Cu	2.1	2.57	0.006	0.0095	2.9
7.6	Cu−O					
11.9	Cu−O					
18.3	Cu−O	1.8	1.87	0.001	0.0062	−1.9
25.2	Cu−O	2.0	1.87	0.006	0.0102	−4.6

^{a}Residual factor. ^{b}Debye−Waller factor. ^{c}The inner potential correction.

Table 3. Structural Parameters of Reduced Cu/SBA-15

Cu loading (%)	shell	N^a	R (Å)	r^a(×10^{-2})	σ^2 (Å^2)^b	ΔE_0 (eV)^c
7.6	Cu−Cu					
11.9	Cu−Cu					
18.3	Cu−Cu	1.4	3.02	0.009	0.0083	3.3
25.2	Cu−Cu	1.8	3.02	0.009	0.0087	2.7
7.6	Cu−O	3.8	1.94	0.001	0.0041	6.2
11.9	Cu−O	3.9	1.94	0.001	0.0021	1.2
18.3	Cu−O	3.9	1.94	0.009	0.0091	1.6
25.2	Cu−O	4.0	1.94	0.009	0.0113	−4.6

^{a}Residual factor. ^{b}Debye−Waller factor. ^{c}The inner potential correction.

magnitude of the Fourier transform of the CuO powder was different from the magnitude of the Fourier transforms of all the calcined Cu/SBA-15 samples (Figure 10B); this result implies that the calcination treatment did not completely form CuO structures on SBA-15. Table 3 shows the coordination number and the bond distance of the Cu/SBA-15 samples reduced at 573 K for 5 h. For the samples with a low Cu loading on SBA-15, the coordination numbers of N_{Cu-Cu} were found to be 7.0 and 7.6 for the samples with 7.6 wt % and 11.9 wt % Cu, respectively. When the Cu content was increased above 18.3 wt %, the Cu−Cu coordination numbers decreased significantly to approximately 2.0. The coordination environment of Cu−O, however, had a bond distance of 1.87 Å for Cu−O, and the coordination number of N_{Cu-O} was approximately 2.0.

3.7. WGS Reaction on Cu/SBA-15 Catalysts. Table 4 compares the amount of CO adsorption, the dispersion, the Cu surface area, and the Cu particle size for all of the Cu/SBA-15

Table 4. Comparison of the Characterization of Cu/SBA-15 and $Cu/ZnO/Al_2O_3$ Catalysts

catalysts	CO adsorption (μmol/g)	dispersion (%)	particle size (nm)	Cu surface area (m^2/g)
20% $Cu/ZnO/Al_2O_3$		15	6.5	23.0
7.6% Cu/SBA-15	18.3	51	2	25.2
11.9% Cu/SBA-15	28.9	43	2	33.2
18.3% Cu/SBA-15	40.6	35	4	41.6
25.2% Cu/SBA-15	53.4	28	6	45.8

and commercial $Cu/ZnO/Al_2O_3$ catalysts. The amount of saturated adsorption of CO on all Cu/SBA-15 catalysts was measured by CO chemisorption at room temperature in a vacuum system. The temperature-dependent TOF of the WGS reaction on the Cu/SBA-15 and $Cu/ZnO/Al_2O_3$ catalysts is shown in Figure 11A. The 7.6 and 11.9 wt % Cu/SBA-15

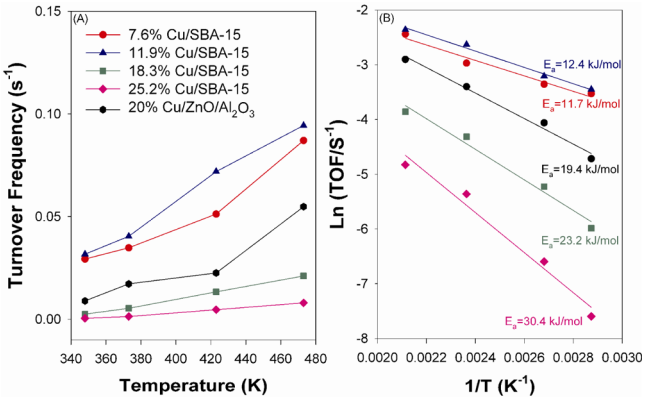

Figure 11. (A) Temperature-dependent TOF of the WGS reaction on Cu/SBA-15 and $Cu/ZnO/Al_2O_3$ catalysts; (B) Arrhenius plots for Cu/SBA-15 and $Cu/ZnO/Al_2O_3$ catalysts at 348−473 K.

catalysts provided a more efficient WGS reaction than did the $Cu/ZnO/Al_2O_3$ catalyst, and the 2-nm Cu particles provided a turnover rate that was significantly higher than that of the large Cu particles on SBA-15. Arrhenius plots and apparent activation energies are shown in Figure 11B. The 7.6 and 11.9 wt % Cu/SBA-15 catalysts effectively provide lower activation energies than other $Cu/ZnO/Al_2O_3$ and Cu/SBA-15 catalysts. Literature has reported the values of TOF and activation energy for WGS reaction on several Cu based catalysts at 473 K, showing that the TOF was in the range of 0.006−0.038 s^{-1} and the activation energy was at 67−86 kJ/mol.[34]

Temperature-dependent IR spectra of CO adsorbed onto the reduced Cu/SBA-15 samples are provided in Figure 12. The IR band of spectrum (a) was assigned to linear CO adsorption on the 7.6 wt % Cu/SBA-15 surface, and the band was fitted by two principal peaks at 2134 cm^{-1} (L_1-CO) and 2119 cm^{-1} (L_2-CO). When the Cu content was increased to 18.3 wt %, a new bridge CO positioned at 1958 cm^{-1} (B_1-CO) was observed. IR bands at wavenumbers greater than 2000 cm^{-1} are characteristic of linearly bound CO; the 2000−1900 cm^{-1} range is usually attributed to bridge CO adsorption. The intensity of the IR of CO adsorption on reduced Cu/SBA-15 gradually decreased as the temperature was increased; however, a small amount of L_1-CO still remained on the Cu surface at 473 K.

dx.doi.org/10.1021/cs400032e | ACS Catal. 2013, 3, 667−677

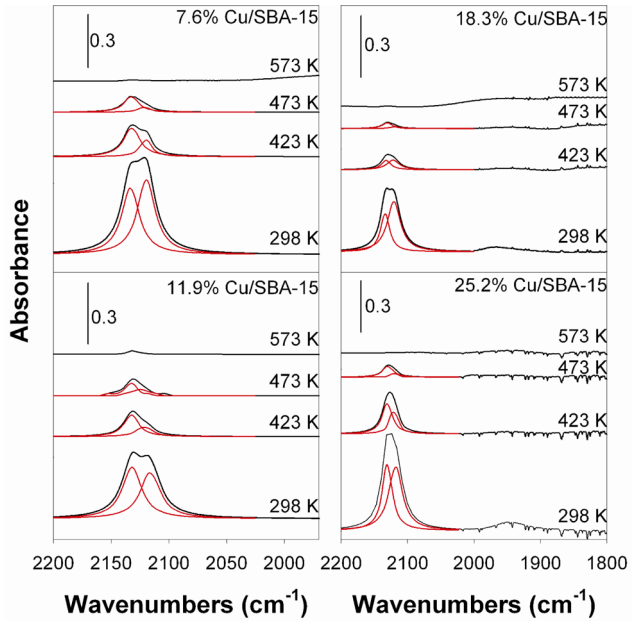

Figure 12. Temperature-dependent IR spectra of CO adsorbed on reduced Cu/SBA-15.

Figure 13 displays the spectra obtained in time-dependent studies of the saturation of adsorbed CO on Cu/SBA-15

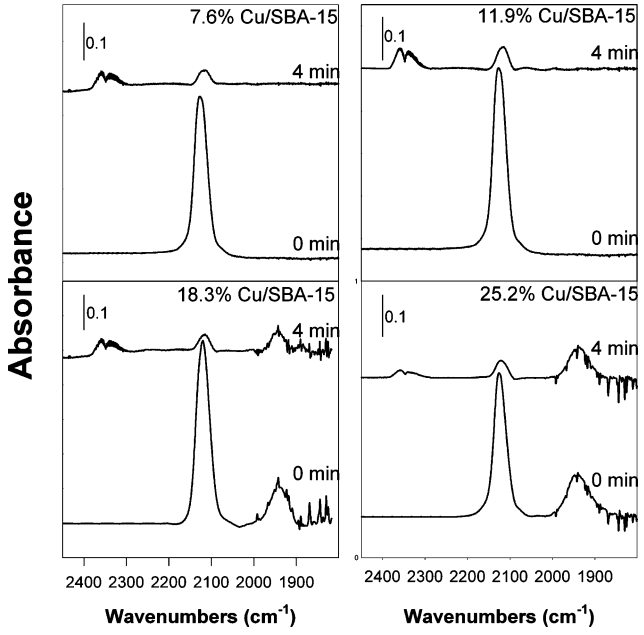

Figure 13. Time dependence of IR spectra for the coadsorption of CO and H_2O on Cu/SBA-15 catalysts at 298 K. All samples were exposed to a stream of CO flowing at 30 mL/min at atmospheric pressure for 30 min, followed by helium flowing at 30 mL/min to purge the CO gas for 30 min; 5 μL of H_2O was then injected into the reaction cell.

catalysts with H_2O at 298 K. Linear CO adsorbed onto the Cu/SBA-15 catalysts rapidly disappeared and led to CO_2 formation (ca. 2340 cm^{-1}) within 4 min at room temperature when 5 μL of H_2O was injected into the reaction cell. However, the bridge-bound CO on 18.3 and 25.2 wt % Cu/SBA-15 remained almost constant in intensity in the course of WGS reaction. The IR bands of the L_1- and L_2-CO species were the major reactive carbonyl components of the WGS reactions on the copper surfaces, and the intensities of these bands decreased over time following the injection of H_2O. The coverage of the L_1- and L_2-CO species versus time is shown in Figure 14. L_1-CO was

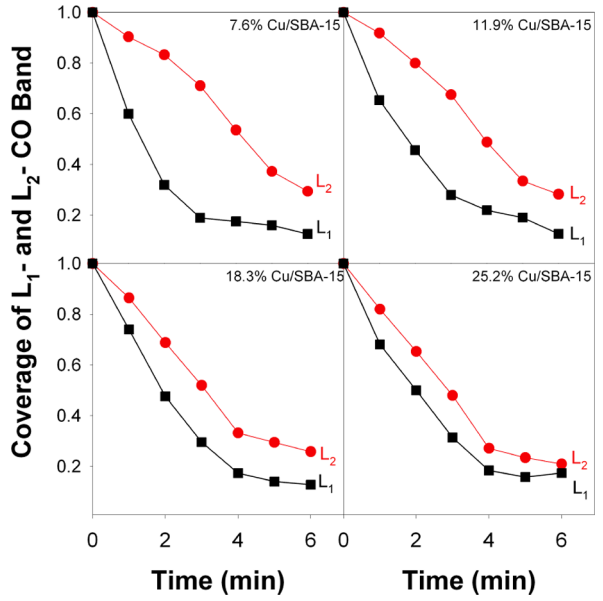

Figure 14. Changes in the coverage of CO species as a function of time for coadsorption of CO and H_2O on Cu/SBA-15 catalysts at 298 K.

clearly consumed faster than the L_2-CO species for all the Cu/SBA-15 catalysts, which implies that CO adsorbed at the L_1-sites reacted more rapidly with adsorbed water than did the L_2-CO species.

Supporting Information, Figure S4 displays the IR spectra of CO adsorbed on 25.2 wt % Cu/SBA-15 with different partial pressure of gaseous CO. IR bands of linear and bridge CO were gradually grown in intensity with CO concentration. The integrated area of linear- and bridge-CO versus CO pressure gave similar linear slopes, implying that both CO adsorption types could have identical extinction coefficient in IR spectroscopy, as all spectra following the Beer–Lambert law ($A = \varepsilon bc$). The amount of CO adsorbed on the B_1-, L_1-, and L_2-sites for all Cu/SBA-15 catalysts based on the relative intensity of IR bands at 298 K in Figure 12 and total amount of CO adsorption is summarized in Table 5. The Cu surface areas of

Table 5. Comparison of the Amount of CO Adsorption on Cu/SBA-15

	CO adsorption (μmol/g)		
catalysts	B_1	L_1	L_2
7.6% Cu/SBA-15	0.0	17.3	11.6
11.9% Cu/SBA-15	0.0	19.9	20.7
18.3% Cu/SBA-15	10.7	20.8	21.9
25.2% Cu/SBA-15	13.2	21.0	25.2

the B_1-, L_1-, and L_2-phases were further determined (Table 6) on the basis of a bridge CO bound to two Cu atoms and a linear CO bound to one Cu atom. The smaller particle size for the 7.6 and 11.9 wt % Cu/SBA-15 catalysts apparently provided a larger L_1-Cu surface area than did high Cu loadings (18.3 and 25.2 wt %).

dx.doi.org/10.1021/cs400032e | ACS Catal. 2013, 3, 667–677

Table 6. Comparison of the Cu Surface Area of Sites for CO Adsorption

	Cu surface area (m^2/g)		
catalysts	B_1	L_1	L_2
7.6% Cu/SBA-15	0.0	15.1	10.1
11.9% Cu/SBA-15	0.0	16.3	16.9
18.3% Cu/SBA-15	13.9	13.5	14.1
25.2% Cu/SBA-15	16.7	13.1	16.0

4. DISCUSSION

4.1. Formation Mechanism of Cu Particles in SBA-15.

For samples with a high Cu loading (18.3 and 25.2 wt %) in SBA-15 that contained −COOH groups, the in situ XRD spectra clearly showed that $Cu_2(OH)_3NO_3$ could be formed over the course of impregnation. Notably, no diffraction signals for $Cu_2(OH)_3NO_3$ were observed in the XRD spectra for the 7.6 and 11.9 wt % Cu^{2+} samples. However, peaks attributable to $Cu_2(OH)_3NO_3$ crystals were observed in the XRD spectra for samples impregnated with 5−15 wt % Cu^{2+} on pure SBA-15 without −COOH groups and SiO_2 (Figure 4). These results suggest that the 7.6 and 11.9 wt % Cu^{2+} samples preferred to coordinate with carboxylic groups rather than form $Cu_2(OH)_3NO_3$ crystals. At low Cu^{2+} concentrations, the coordination number of 4.0 for N_{Cu-O} could be ascribed to Cu^{2+} coordinated with carboxylic acid O^- groups. We propose that $Cu_2(OH)_3NO_3$ crystals formed at high impregnation concentrations might be due to initial Cu^{2+} ions saturating the −COOH binding sites.

The $Cu_2(OH)_3NO_3$ is a prototypical layered solid characterized by planar $[Cu_2(OH)_3]^+$ layers stacked with hydrogen bonding.[35−37] This system contains stacked $Cu_2(OH)_4$ sheets, with NO_3^- ions in the interlayer replacing 1/4 of the OH^- ions. Fujita et al. have provided structural parameters for C−O bonding in $Cu_2(OH)_3NO_3$ crystals using EXAFS analysis, which revealed that the coordination number of N_{Cu-O} was 4.0 and that the bond distance was 1.98 Å.[35] In $Cu_2(OH)_3NO_3$ single crystals, Cu−Cu bonding exhibited a coordination number of 2.0 and a bond distance of 3.02 Å.[37] In the present study, the EXAFS results for C−O coordination in samples with 18.3 and 25.2 wt % Cu^{2+} (as listed in Table 1) were similar to the data from Fujita's analysis. However, we could not analyze the Cu−Cu bonding from the experimental data, even though the crystalline $Cu_2(OH)_3NO_3$ phase at high Cu loadings was identified in the XRD spectra. We assume that the analysis of the EXAFS spectra for samples with high Cu loadings might contain average data derived from the mechanism of $Cu_2(OH)_3NO_3$ formation and the process of Cu^{2+} ions binding with carboxylic acid groups.

The EXAFS analysis of all impregnated samples calcined at 573 K for 5 h showed coordination numbers of 3.8−4.0 and Cu−O bond lengths of 1.94 Å (Table 2). In the present work, we could not collect data on Cu−Cu bonding for Cu loadings less than 11.9 wt %. When Cu loading was increased to 18.3 and 25.2 wt %, the coordination numbers for N_{Cu-Cu} less than 2.0 were present. The first coordination shell of Cu−O in CuO has been reported to be at 1.96 Å, and the average number of oxide ions around Cu^{2+} has been reported to be 4.0.[29] Therefore, the Cu−Cu bond in CuO could provide a bond distance of 2.9 Å and a coordination number of 4.0. However, the average data for Cu oxides in SBA-15 (shown in Figure 10 and Table 2) did not completely match the data for the typical CuO structure. The in situ XRD spectra revealed no diffraction peaks for Cu oxides at loadings less than 11.9 wt %, but 2-nm Cu nanoparticles could still be obtained through reduction. In Table 3, the coordination numbers of Cu−Cu bonds on the reduced samples with 7.6 and 11.9 wt % Cu (N = 7.0 or 7.6) were low compared with the bulk coordination number (N = 12),[38] which, according to the literature data, implies that the Cu particle size may be approximately 1.5 nm.[39]

The UV−vis spectra of the calcined Cu/SBA-15 samples may indicate the coordination environment of the Cu^{2+} species in SBA-15 (Figure 3). For the 7.6 wt % CuO/SBA-15 sample, linear $[Cu^{\delta+}\cdots O^{\delta-}\cdots Cu^{\delta+}]_n$ species formed during calcination were the dominant Cu oxide phase in SBA-15, as evidenced by the band from 350 to 650 nm. The formation of $[Cu^{\delta+}\cdots O^{\delta-}\cdots Cu^{\delta+}]_n$ species is associated with Cu^{2+} ions coordinating with carboxylic acid groups, which explains the absence of a significant Fourier component for Cu−Cu backscattering. We propose that $[Cu^{\delta+}\cdots O^{\delta-}\cdots Cu^{\delta+}]_n$ nanoclusters existed in the channels of SBA-15. The intensity of the LMCT band at 290 nm increased as the $[Cu^{\delta+}\cdots O^{\delta-}\cdots Cu^{\delta+}]_n$ structure vanished, which indicated that bulky CuO likely aggregated from Cu^{2+} ions during calcination because of the high Cu^{2+} concentration in SBA-15. On the basis of the XRD spectra, calcination at 573 K led to a mixture of CuO and a small amount of $Cu_2(OH)_3NO_3$ crystals in SBA-15 for the 18.3 and 25.2 wt % Cu^{2+} samples. The formation of this mixture may explain why we did not observe the typical CuO structure in the EXAFS spectra. The XANES spectra clearly show that H_2 treatment at 573 K can reduce samples with 7.6 and 11.9 wt % Cu to metallic Cu. However, the same reduction pretreatment was unable to fully reduce samples with a higher Cu content (18.3 and 25.2 wt %). After the spectra were fit using the FEFF7 software, the coordination numbers of Cu−O and Cu−Cu were found to be 1.8−2.0 and 2.0−2.1, respectively, whereas the bond distances of Cu−O and Cu−Cu were 1.87 and 2.55−2.57 Å, respectively. These results implied that the interaction between Cu and O may occur in samples with high Cu loading after they were reduced at 573 K.

The TPR profile of the oxidized Cu/SBA-15 catalyst featured reduction peaks at 533 and 703 K for samples with a high Cu loading (18.3 wt % and 25.2 wt %), as shown in Figure 1. In general, the reduction temperature of small CuO particles was lower than that of bulk CuO.[40] Some literature reports have indicated that the reduction temperature of a well-dispersed (3−5 nm) CuO/SiO_2 catalyst prepared by an ion-exchange method may be less than 423 K.[41] However, this ion-exchange method may result in the formation of Cu−O−Si species during the preparation of a Cu/SiO_2 catalyst. The reduction of Cu^{2+} for Cu−O−Si species required a temperature greater than 873 K.[41] Thus, the low-temperature peak at 423 K in the present TPR profiles (Figure 1) could be reasonably assigned to a one-step reduction of Cu^{2+} to Cu^0 in highly dispersed CuO particles. The second peak at the higher temperature was attributed to a reduction path from Cu^{2+} to Cu^0 because of strong interactions between copper and the SBA-15 surface. However, the TPR profile of the 25.2 wt % Cu^{2+}/SBA-15 without calcination did not show high-temperature reduction at 703 K. This result suggests that the strong interaction between Cu and SBA-15 is the result of calcination. In fact, the similar result of Cu^+ interacting strongly with the SBA-15 support for Au−Cu/SBA-15 catalysts has been also reported in literature.[42]

The sample with 13 wt % Cu loaded in pure SBA-15 without −COOH groups exhibited an average particle size of 7.6 nm in

dx.doi.org/10.1021/cs400032e | ACS Catal. 2013, 3, 667−677

our previous study.[19] The SBA-15 with carboxylic groups used in this paper may contain nanosized Cu particles in the SBA-15 material because of the attraction between carboxylic groups and Cu^{2+} ions. In our experience, however, it is usually difficult to synthesize Cu particles smaller than 3 nm in diameter when the Cu loading is greater than 10 wt %. In this study, SBA-15 with carboxylic groups and 11.9 wt % Cu formed 2-nm Cu particles. Even at 25.2 wt % Cu, the Cu particles were still approximately 6 nm in diameter.

4.2. Active sites on Cu/SBA-15. The IR spectra of CO adsorbed on Cu/SBA-15 have been proposed to exhibit two major peaks at 2134 cm^{-1} (L_1-CO) and 2119 cm^{-1} (L_2-CO) for all of the Cu/SBA-15 surfaces. Bridge-type CO adsorption on the reduced Cu/SBA-15 surface can be enhanced with increased Cu loading. The assignment of the IR bands for linearly adsorbed CO on a reduced Cu surface has been proposed by others.[40−42] IR bands below 2100 cm^{-1} were assigned to CO adsorbed on low index planes, such as the (111) and (100) faces, whereas the band at 2102−2118 cm^{-1} was assigned to CO adsorbed at imperfect sites, such as step and edge sites.[41,43,44] Bands above 2120 cm^{-1} may arise from CO adsorbed on highly dispersed and/or isolated copper particles.[45−47] However, stretching frequencies of CO adsorbed on copper have also been found to occur in different regions for each oxidation state. In general, peaks located above 2140 cm^{-1} can be attributed to Cu^{2+} sites.[48−53] Furthermore, the band for CO adsorbed on Cu^{+} sites has been reported in the 2110−2135 cm^{-1} range.[48−53]

Assignments of IR spectra in the literatures thus suggest that the L_2-CO depended on CO adsorbed on defect sites, but clear differences were not detected between the L_1-CO in terms of the electronic and structural effects of copper. The XANES and EXAFS spectra have clearly shown that the fully reduced metallic Cu particles could be formed after H_2-treatment at 573 K for 7.6 and 11.9 wt % Cu/SBA-15 catalysts. However, the Cu−O coordination may occur on high Cu loading samples. Supporting Information, Figure S5 reveals the temperature dependent-IR spectra of CO adsorbed on the reduced 25.2 wt % Cu/SBA-15 oxidized by N_2O stream (30 mL/min) for 15 s at 353 K. It can see that the bridge-bound CO was absent on the slightly oxidized Cu/SBA-15, and the higher stretching frequency of 2134 cm^{-1} (L_1-CO) could strongly bind on the Cu surface even at 573 K. Supporting Information, Figure S6A displays the IR spectra of coadsorbed CO and H_2O performed on the slightly oxidized Cu/SBA-15 for comparison with 25.2 wt % reduced Cu/SBA-15 (Figure 13). It was found that the intensity of adsorbed CO did not significantly decrease within 6 min. The comparison of consumption of CO coverage on reduced and slightly oxidized Cu/SBA-15 was shown in Supporting Information, Figure S6B, revealing that the slightly oxidized Cu/SBA-15 offered much less efficiency for WGS reaction. These results suggested that few Cu^{+} species formed on the 25.2 wt % Cu/SBA-15 could cause significant difference in the IR spectra of CO adsorption and efficiency for WGS reaction, comparing with the reduced Cu sample. Thus, we assumed that the L_1-sites on Cu/SBA-15 ascribed to oxidized Cu^{+} species could be excluded.

In general, CO adsorbed on reduced or oxidized Cu surfaces prefers stable linear adsorption on top sites, which produces IR stretching bands for CO above 2000 cm^{-1}. Bridge-bound CO adsorbed on the Cu surface (IR spectrum below 2000 cm^{-1}) is usually only observed at low temperatures because of the low adsorption energy. We found it difficult to observe bridge-bound CO in the IR spectra of Cu-based catalysts at room temperature. In the present work, the high loading of Cu on SBA-15 led to the presence of bridge CO on the Cu surface. However, Liu et al. studied CO adsorbed on a $Cu/ZnO/Al_2O_3$ catalyst and demonstrated that bridge-bound CO could form on the surface of a $CuZn_x$ alloy (at ca. 1975 and 1920 cm^{-1}).[54] In addition, several reports have indicated that bridge CO adsorption can occur on bimetallic Cu−Pt or Cu−Fe surfaces.[55,56] Other authors have proposed that new sites created on the interface of bimetallic Cu systems influence the CO chemisorption bond type due to a change in the d-band structure.[55] The formation of bridge sites on Cu/SBA-15 is not clearly understood, but we assume that the formation of the CO peak at 1958 cm^{-1} (B_1-CO) is related to the strong interaction between SiOH and metallic Cu.

The results shown in Figure 13 indicate that the WGS reaction occurs mainly at L_1- and L_2-sites for CO adsorption but that B_1-CO was evidently insensitive to WGS reactions. The respective carbonyl species (L_1- and L_2-CO) displayed large differences in the rates at which they underwent the WGS reaction. The rate of coverage loss for L_1-CO was evidently faster than that for L_2-CO when H_2O was added to CO-covered Cu/SBA-15 at 298 K. This result implied that L_1-sites were highly active in the WGS reaction. The CO adsorbed at L_2 sites, that is, defect sites (sites that give rise to CO stretching at 2119 cm^{-1}), were still available for the WGS reaction but proved to be less efficient. On the basis of the data in Table 6, we propose that the high efficiency of the WGS reaction on 7.6 and 11.9 wt % Cu/SBA-15 may be ascribed to the larger Cu surface area for L_1-sites. The presence of B_1 sites on 18.3 and 25.2 wt % Cu/SBA-15 catalysts might lead to low reaction rate in WGS reaction. The presence of abundant L_1-sites on small 2 nm Cu nanoparticles leads to a highly efficient WGS reaction.

5. CONCLUSION

In this work, SBA-15 functionalized with carboxylic acid groups was used as a support to synthesize Cu nanoparticles 2−6 nm in size with 7.6−25.2 wt % Cu concentrations. At low Cu^{2+} impregnation concentrations (i.e., less than 11.9 wt %), Cu^{2+} ions coordinate with carboxylic acid O^{-} groups. The UV−vis spectra of calcined Cu/SBA-15 samples show a coordination environment of Cu^{2+} oxides in the SBA-15 structure with linear chain $[Cu^{\delta+}\cdots O^{\delta-}\cdots Cu^{\delta+}]_n$ species formed during the calcination of 7.6 and 11.9 wt % CuO/SBA-15 samples. We propose that $[Cu^{\delta+}\cdots O^{\delta-}\cdots Cu^{\delta+}]_n$ nanoclusters insert into the channels of SBA-15. Crystals of $Cu_2(OH)_3NO_3$ formed when high concentrations of Cu^{2+} ions were impregnated in SBA-15. The $Cu_2(OH)_3NO_3$, which is the dominant intermediate species before bulky CuO, is formed. The slightly oxidized Cu/SBA-15 that contains 18.3 and 25.2 wt % Cu loading after reduction at 300 °C is due to the interface between SiOH and metallic Cu.

Nanoscale 2-nm Cu particles provided highly efficient WGS reactions compared with 20% $Cu/ZnO/Al_2O_3$ and large Cu particles on SBA-15. The IR spectra of CO adsorbed onto Cu/SBA-15 catalysts revealed two major active sites on the copper surface that contribute to the WGS reaction: highly dispersed Cu particles (sites for L_1-CO with an IR peak at 2134 cm^{-1}) and defect sites (sites for L_2-CO with an IR peak at 2119 cm^{-1}). We conclude that the WGS reaction mainly occurs at the highly dispersed Cu particles and/or isolated Cu atoms. The presence of abundant L_1-sites on small 2 nm Cu nanoparticles leads to a highly efficient WGS reaction.

dx.doi.org/10.1021/cs400032e | ACS Catal. 2013, 3, 667−677

■ ASSOCIATED CONTENT

Supporting Information

Further details are given in Figures S1−S6. This material is available free of charge via the Internet at http://pubs.acs.org.

■ AUTHOR INFORMATION

Corresponding Author

*E-mail: cschen@mail.cgu.edu.tw (C.S.C.). Phone: +886-32118800, x5685 (C.S.C.). Fax: +886-32118700 (C.S.C.).

Notes

The authors declare no competing financial interest.

■ ACKNOWLEDGMENTS

Financial support from the National Science Council of the Republic of China (NSC 100-2113-M-182-001-MY3) and Chang-Gung Memorial Hospital (CMRPD190042) are gratefully acknowledged. We are also grateful for access to in situ X-ray absorption spectroscopy (BL17C1) and in situ XRD measurements (BL01C2) collected at the National Synchrotron Radiation Research Center (NSRRC).

■ REFERENCES

(1) White, B.; Yin, M.; Hall, A.; Le, D.; Stolbov, S.; Rahman, T.; Turro, N.; O'Brien, S. *Nano Lett.* **2006**, *6*, 2095−2098.
(2) Garitaonandia, J. S.; Insausti, M.; Goikolea, E.; Suzuki, M.; Cashion, J. D.; Kawamura, N.; Ohsawa, H.; Muro, I. G. D.; Suzuki, K.; Plazaola, F.; Rojo, T. *Nano Lett.* **2008**, *8*, 661−667.
(3) Pászti, Z.; Petö, G.; Horváth, Z. E.; Karacs, A.; Guczi, L. *J. Phys. Chem. B* **1997**, *101*, 2109−2115.
(4) Chen, P.; Wu, X.; Lin, J.; Tan, K. L. *J. Phys. Chem. B* **1999**, *103*, 4559−4561.
(5) Porte, L.; Phaner-Goutorbe, M.; Guigner, J. M.; Bertolini, J. C. *Surf. Sci.* **1999**, *424*, 262−270.
(6) Qiao, B.; Wang, A.; Yang, X.; Allard, L. F.; Jiang, Z.; Cui, Y.; Liu, J.; Li, J.; Zhang, T. *Nat. Chem.* **2011**, *3*, 634−641.
(7) Berndt, H.; Martin, A.; Brückner, A.; Schreier, E.; Muller, D.; Kosslick, H.; Wolf, G. U.; Lücke, B. *J. Catal.* **2000**, *191*, 384−400.
(8) Fornés, V.; López, C.; López, H. H.; Martínez, A. *Appl. Catal., A* **2003**, *249*, 345−354.
(9) Baltes, M.; Cassiers, K.; Van Der Voort, P.; Weckhuysen, B. M.; Schoonheydt, R. A.; Vansant, E. F. *J. Catal.* **2001**, *197*, 160−171.
(10) Du, G.; Lim, S.; Pinault, M.; Wang, C.; Fang, F.; Pfefferle, L.; Haller, G. L. *J. Catal.* **2008**, *253*, 74−90.
(11) Tu, C. H.; Wang, A. Q.; Zheng, M. Y.; Wang, X. D.; Zhang, T. *Appl. Catal., A* **2006**, *297*, 40−47.
(12) Yoshida, K.; Arellano, C. G.; Luque, R.; Gai, P. L. *Appl. Catal., A* **2010**, *379*, 38−44.
(13) Chanquía, C. M.; Sapag, K.; Rodríguez-Castellón, E.; Herrero, E. R.; Eimer, G. A. *J. Phys. Chem. C* **2010**, *114*, 1481−1490.
(14) Huang, J.; Wang, M.; Zhang, S.; Hu, B.; Li, H. *J. Phys. Chem. C* **2011**, *115*, 22514−22522.
(15) Takai, A.; Doi, Y.; Yamauchi, Y.; Kuroda, K. *J. Phys. Chem. C* **2010**, *114*, 7586−7593.
(16) Zhao, A.; Zhang, X.; Chen, X.; Guan, J.; Liang, C. *J. Phys. Chem. C* **2010**, *114*, 3962−3967.
(17) Yin, A.; Guo, X.; Dai, W. L.; Fan, K. *J. Phys. Chem. C* **2010**, *114*, 8523−8532.
(18) Gu, J.; Huang, Y.; Elangovan, S. P.; Li, Y.; Zhao, W.; Toshio, I.; Yamazaki, Y.; Shi, J. *J. Phys. Chem. C* **2011**, *115*, 21211−21217.
(19) Liu, Y. M.; Xie, S. H.; Cao, Y.; He, H. Y.; Fan, K. N. *J. Phys. Chem. C* **2010**, *114*, 5941−5946.
(20) Chen, C. S.; Chen, C. C.; Chen, C. T.; Kao, H. M. *Chem. Commun* **2011**, *47*, 2288−2290.
(21) Chen, C. S.; Chen, C. C.; Lai, T. W.; Wu, J. H.; Chen, C. H.; Lee, J. F. *J. Phys. Chem. C* **2011**, *115*, 12891−12900.
(22) Chen, C. S.; Wu, J. H.; Lai, T. W. *J. Phys. Chem. C* **2010**, *114*, 15021−15028.
(23) Chen, C. S.; Lai, T. W.; Chen, C. C. *J. Catal.* **2010**, *273*, 18−28.
(24) Chen, C. S.; Lin, J. H.; Lai, T. W.; Li, B. H. *J. Catal.* **2009**, *263*, 155−166.
(25) Chen, C. S.; Lin, J. H.; Lai, T. W. *Chem. Commun.* **2008**, 4983−4985.
(26) Chen, C. S.; Lin, J. H.; You, J. H.; Chen, C. R. *J. Am. Chem. Soc.* **2006**, *128*, 15950−15951.
(27) Nakamura, J.; Nakamura, I.; Uchijima, T.; Kanai, Y.; Watanabe, T.; Saito, M.; Fujitani, T. *J. Catal.* **1996**, *160*, 65−75.
(28) Marchi, A. J.; Fierro, J. L. G.; Santamaria, J.; Mozon, A. *Appl. Catal., A* **1996**, *142*, 375−386.
(29) Chanquía, C. M.; Andrini, L.; Fernández, J. D.; Crivello, M. E.; Requejo, F. G.; Herrero, E. R.; Eimer, G. A. *J. Phys. Chem. C* **2010**, *114*, 12221−12229.
(30) Velu, S.; Suzuki, K.; Okazaki, M.; Kapoor, M. P.; Osaki, T.; Ohashi, F. *J. Catal.* **2000**, *194*, 373−384.
(31) Munnik, P.; Wolters, M.; Gabrielsson, A.; Pollington, S. D.; Headdock, G.; Bitter, J. H.; de Jongh, P. E.; de Jong, K. P. *J. Phys. Chem. C* **2011**, *115*, 14698−14706.
(32) Kim, W. B.; Park, E. D.; Lee, C. W.; Lee, J. S. *J. Catal.* **2003**, *218*, 334−347.
(33) Kau, L.-S.; Spira-Solomon, D. J.; Penner-Hahn, J. E.; Hodgson, K. O.; Solomon, E. I. *J. Am. Chem. Soc.* **1987**, *109*, 6433−6442.
(34) Korybkina, N. A.; Phatak, A. A.; Ruettinger, W. F.; Farrauto, R. J.; Ribeiro, F. H. *J. Catal.* **2003**, *217*, 233−239.
(35) Massobrio, C.; Rabu, P.; Drillon, M. *J. Phys. Chem. B* **1999**, *103*, 9387−9391.
(36) Ruiz, E.; Llunell, M.; Cano, J.; Rabu, P.; Drillon, M.; Massobrio, C. *J. Phys. Chem. B* **2006**, *110*, 115−118.
(37) Fujita, W.; Awaga, K.; Yokoyama, T. *Inorg. Chem.* **1997**, *36*, 196−199.
(38) Bera, P.; Priolkar, K. R.; Sarode, P. R.; Hegde, M. S.; Emura, S.; Kumashiro, R.; Lalla, N. P. *Chem. Mater.* **2002**, *14*, 3591−3601.
(39) Knapp, R.; Wyrzgol, S. A.; Jentys, A.; Lercher, J. A. *J. Catal.* **2010**, *276*, 280−291.
(40) Chen, L. F.; Guo, P. J.; Qiao, M. H.; Yan, S. R.; Li, H. X.; Shen, W.; Xu, H. L.; Fan, K. N. *J. Catal.* **2008**, *257*, 172−180.
(41) Marchi, A. J.; Fierro, J. L. G.; Santamaría, J.; Mozón, A. *Appl. Catal., A* **1996**, *142*, 375−386.
(42) Liu, X.; Wang, A.; Li, L.; Zhang, T.; Mou, C. Y.; Lee, J. F. *J. Catal.* **2011**, *278*, 288−296.
(43) Hollins, P. *Surf. Sci. Rep.* **1992**, *16*, 51−94.
(44) Boccuzzi, F.; Chiorino, A.; Martra, G.; Gargano, M.; Ravasio, N.; Carrozzini, B. *J. Catal.* **1997**, *165*, 129−139.
(45) Coloma, F.; Marquez, F.; Rochester, C. H.; Anderson, J. A. *Phys. Chem. Chem. Phys.* **2000**, *2*, 5320−5327.
(46) Boccuzzi, F.; Coluccia, S.; Martra, G.; Ravasio, N. *J. Catal.* **1999**, *184*, 316−326.
(47) Boccuzzi, F.; Martra, G.; Partipilo Papalia, C.; Ravasio, N. *J. Catal.* **1999**, *184*, 327−334.
(48) Dandekar, A.; Vannice, M. A. *J. Catal.* **1998**, *178*, 621−639.
(49) Sakakini, B. H.; Tabatabaei, J.; Watson, M. J.; Waugh, K. C. *J. Mol. Catal. A* **2000**, *162*, 297−306.
(50) Larrubia Vargas, M. A.; Busca, G.; Costantino, U.; Marmottini, F.; Montanari, T.; Patrono, P.; Pinzari, F.; Ramis, G. *J. Mol. Catal. A* **2007**, *266*, 188−197.
(51) Topsøe, N. Y.; Topsøe, H. *J. Mol. Catal. A* **1999**, *141*, 95−105.
(52) Kannan, S.; Venkov, Tz.; Hadjiivanov, K.; Knözinger, H. *Langmuir* **2004**, *20*, 730−736.
(53) Konduru, M. V.; Chuang, S. S. C. *J. Catal.* **2000**, *196*, 271−286.
(54) Liu, Z.; Rittermeier, A.; Becker, M.; Kähler, K.; Löffler, E.; Muhler, M. *Langmuir* **2011**, *27*, 4728−4733.
(55) Wadayama, T.; Jubo, K.; Yamashita, T.; Tanabe, T.; Hatta, A. *J. Phys. Chem. B* **2003**, *107*, 3768−3773.
(56) Shpiro, E. S.; Tkachenko, O. P.; Jaeger, N. I.; Schulz-Ekloff, G.; Grünert, W. *J. Phys. Chem. B* **1998**, *102*, 3798−3805.